

Observation of Impurity-Induced Scale-Free Localization in a Disordered Non-Hermitian Electrical Circuit

Hao Wang,^{1,*} Jin Liu,^{1,*} Tao Liu,^{1,†} and Wen-Bo Ju^{1,‡}

¹*School of Physics and Optoelectronics, South China University of Technology, Guangzhou 510640, China*
(Dated: January 16, 2025)

One of unique features of non-Hermitian systems is the extreme sensitive to their boundary conditions, e.g., the emergence of non-Hermitian skin effect (NHSE) under the open boundary conditions, where most of bulk states become localized at the boundaries. In the presence of impurities, the scale-free localization can appear, which is qualitatively distinct from the NHSE. Here, we experimentally design a disordered non-Hermitian electrical circuits in the presence of a single non-Hermitian impurity and the nonreciprocal hopping. We observe the anomalous scale-free accumulation of eigenstates, opposite to the bulk hopping direction. The experimental results open the door to further explore the anomalous skin effects in non-Hermitian electrical circuits.

I. INTRODUCTION

Growing efforts have been invested to intriguing phenomenon of non-Hermitian systems in recent year¹⁻⁴⁶. One of unique features in non-Hermitian systems is the non-Hermitian skin effect (NHSE)⁷⁻¹³. This effect is characterized by an extreme sensitivity of eigenspectra to boundary conditions, where most of bulk modes become localized at the boundaries under open boundary conditions (OBCs). A lot of exciting non-Hermitian phenomena without their Hermitian counterparts are related to the NHSE, e.g., breakdown of conventional Bloch band theory⁷, scale-free localization³¹, and disorder-free entanglement phase transitions³⁷. The NHSEs have been experimentally observed in many physical systems and have also shown potential applications in sensors due to the extreme sensitivity to the boundary conditions⁴⁷⁻⁴⁹.

For NHSE, the localization length of bulk modes is usually independent of the system's size under OBCs. Recently, an anomalous skin localization, dubbed scale-free localization, was found and extensively explored in non-Hermitian system^{25,31,50-55}. Unlike the conventional NHSE, the localization length of scale-free modes relies on the system size, and the localization direction is not indicated by the bulk. This intriguing localization phenomenon has been largely investigated in various non-Hermitian systems^{25,31,50-55}. Recently, the scale-free localization has been experimentally observed in an electrical circuit with a Hermitian lattice subjected to a parity-time-symmetric non-Hermitian defect⁵⁴. While, the experimental observation of the scale-free localization, resulting from the interplay of nonreciprocal hopping in the bulk and the single impurity, is still lacking.

An electrical circuit has become a powerful platform to realize topological structures even with complicated lattice geometries, e.g., higher-order topological Anderson insulator, novel topological states in hyperbolic lattices, and among others⁵⁶⁻⁶². Due to the design flexibility, the nonreciprocal hopping can be easily realized by using operational amplifiers arranged as impedance converters through current inversion (INIC)⁶³. Therefore, the electrical circuits have been utilized to realize novel non-Hermitian phenomena⁶³⁻⁶⁹. In this work, we experimentally designed the non-Hermitian electrical circuit in the presence of the nonreciprocal hopping, a single non-Hermitian impurity and onsite disorder. We measure and observe the scale-free localization in the disordered non-Hermitian chain.

Such anomalous scale-free accumulations of eigenstates are controlled by the single non-Hermitian impurity, and their localization direction can be opposite to the bulk hopping direction. Our experiment verifies the existence of the anomalous skin effects induced by the single impurity in the nonreciprocal systems, and the results open the door to further explore the interesting localization phenomena in non-Hermitian electrical circuits.

II. MODEL AND NON-HERMITIAN ELECTRICAL CIRCUIT

In order to study the anomalous skin effect due to the interplay of disorder and impurity, we consider the disordered Hatano-Nelson (HN) chain in the presence of a single non-Hermitian impurity, with its Hamiltonian reading⁵⁵

$$\mathcal{H} = \sum_{n=1}^{N-1} [(t + \gamma) |n+1\rangle \langle n| + (t - \gamma) |n\rangle \langle n+1|] + \sum_{n=1}^N V_n |n\rangle \langle n| + (v + \delta) |1\rangle \langle N| + (v - \delta) |N\rangle \langle 1|, \quad (1)$$

where $t \pm \gamma$ indicate the asymmetric hopping strengths, V_n is onsite disorder potential, sampled in a random uniform distribution $[-V, V]$, and $v \pm \delta$ are the asymmetric hopping strengths between the first and last sites, severing as a single non-Hermitian impurity [see Fig. 1(a)]. By controlling the impurity's parameters $v \pm \delta$ in the presence of the disorder, one can observe anomalous skin-localization phenomena⁵⁵, where the system undergoes Anderson localization and scale-free skin localization, as indicated by the phase diagram in Fig. 1(b). The phase diagram is obtained by calculating the mean center of mass (mcom), which is defined as the amplitude squared of all right eigenvectors $|\psi_{R,n}\rangle$, averaged over many disorder realizations N_r ⁵⁵, i.e.,

$$\text{mcom} = \frac{\sum_{j=1}^N j \langle \mathcal{A}(j) \rangle_V}{\sum_{j=1}^N \langle \mathcal{A}(j) \rangle_V}, \quad (2)$$

with

$$\langle \mathcal{A}(j) \rangle_V = \left\langle \frac{1}{N} \sum_{n=1}^N (|\langle j | \psi_{R,n} \rangle|^2) \right\rangle_V. \quad (3)$$

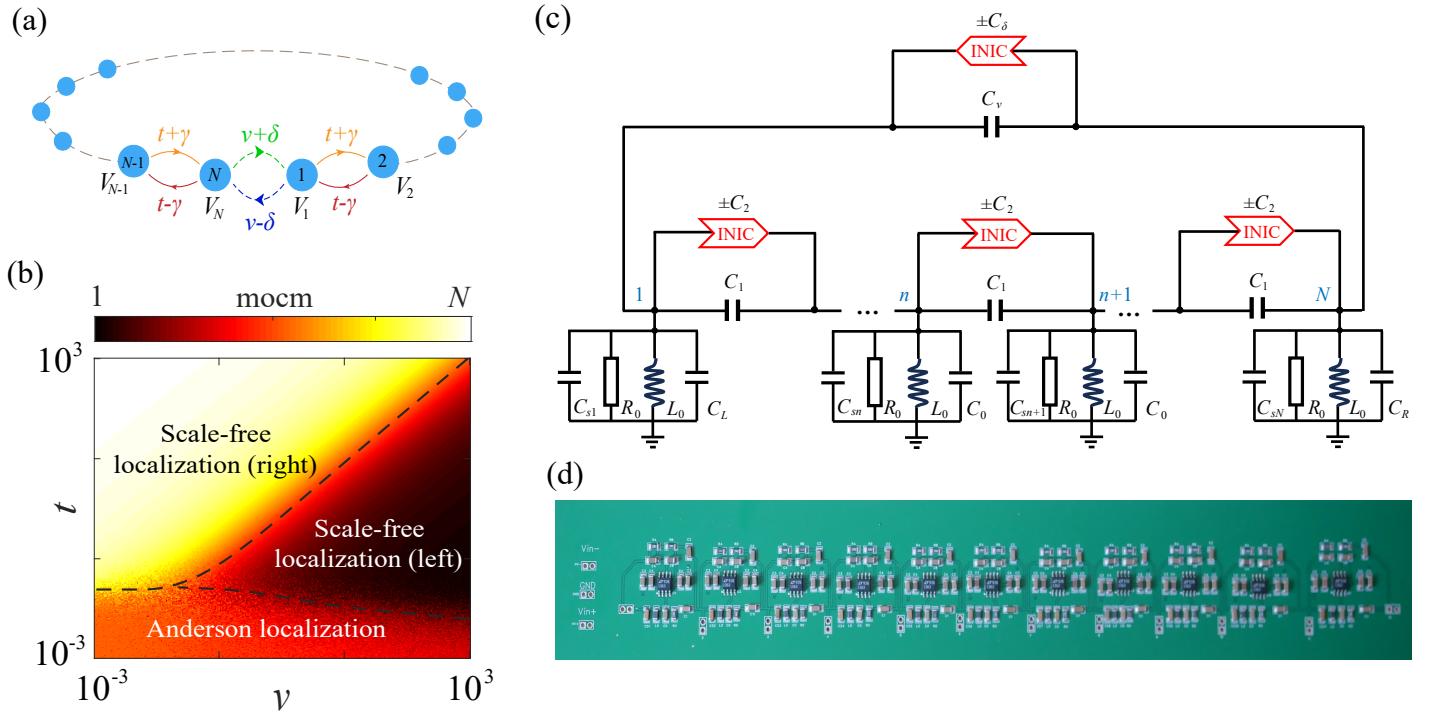


FIG. 1. (a) Schematic of HN model in the presence of onsite disorder and a single non-Hermitian impurity. $t \pm \gamma$ denotes the nonreciprocal hopping strength, $v \pm \delta$ is the nonreciprocal hopping strength between the first and last sites, severing as a single non-Hermitian impurity, and $V_n \in [-V, V]$ is the random onsite potential with $V = 0.05$. (b) Phase diagram of the model as functions of t and v with $t = \gamma$ and $v = \delta \neq 0$. (c) Electrical circuit implementation of the model. The nodes are interconnected by INIC and capacitors in parallel, achieving nonreciprocal hopping. (d) Photographne of the experimental circuit board.

Here, $\langle \cdot \rangle_V$ indicates disorder averages.

The nonreciprocal hopping typically leads to non-Hermitian skin effects in the clean system. While, the scale-free localization in the presence of a single non-Hermitian impurity is distinct from the non-Hermitian skin effect, where its localization is not dictated by the bulk, and the localization length is proportional to the system size⁵⁵. Furthermore, the localization at the left or right boundary of the chain is controlled by the impurity hopping strength in the 1D disordered HN chain [see Fig. 1(b)]. Note that such anomalous skin-localization feature is determined by the interplay of bulk hopping strength and the single non-Hermitian impurity, but it is stabilized to a nonmonotonic localization behavior as a function of the hopping terms by the random disorder⁵⁵, as shown in Fig. 1(b).

In order to experimentally observe the anomalous skin-localization phenomena due to the interplay of a single non-Hermitian impurity and the bulk nonreciprocal hopping, we design non-Hermitian electrical circuits, corresponding to the model in Eq. (1). Figure 1(c) plots the electrical circuit network, where the nonreciprocal hopping between nodes n and $n + 1$ is realized by the negative impedance converters through current inversions (INICs)⁶³. Figure 1(d) shows the experimental circuit board, where the first node and the last node are connected by the external wires acting as the single non-Hermitian impurity. The disorder term V_n in Eq. (1) is introduced by the grounded capacitor C_{sn} ($n = 1, 2, \dots, N$) and the tolerance of the grounded inductance L_0 [see Fig. 1(c)]. The model in Eq. (1) is represented by the circuit Laplacian $J(\omega)$ of the circuit⁶⁴. The Laplacian is defined as the grounded-voltage vector \mathbf{V} to the vector \mathbf{I} of input current by $\mathbf{I}(\omega) = J(\omega)\mathbf{V}(\omega)$. As

shown in Fig. 1(c), the circuit Laplacian reads (see Appendix A)

$$\begin{aligned}
 J = i\omega \sum_{n=1}^{N-1} & (-C_2 - C_1) |n+1\rangle \langle n| + (C_2 - C_1) |n\rangle \langle n+1| \\
 & + (-C_\delta - C_v) |1\rangle \langle N| + (C_\delta - C_v) |N\rangle \langle 1| \\
 & + i\omega \sum_{n=1}^n \left[C_{sn} - \frac{C_S}{2} - \varepsilon(\omega) \right] |n\rangle \langle n|, \quad (4)
 \end{aligned}$$

with

$$\varepsilon(\omega) = \frac{1}{\omega^2 L_0} - 2C_1 - C_0 - \frac{C_S}{2} + \frac{i}{\omega R_0}, \quad (5)$$

where C_{sn} signifies a grounded capacitor at the node n within the range $[0, C_S]$. By further writing J as $J = i\omega[\mathcal{H} - \varepsilon(\omega)]$, one found that J and \mathcal{H} share the same eigenstates, if we set $\pm C_2 - C_1 = t \pm \gamma$, $\pm C_\delta - C_v = v \pm \delta$, and $C_{sn} - C_S/2 = V_n$. The eigenvalues and eigenstates of J can be obtained by measuring the voltage response at the circuit nodes.

III. ELECTRICAL-CIRCUIT SIMULATION OF SCALE-FREE LOCALIZATION

It has shown that the single non-Hermitian impurity can induce a scale-free accumulation of all eigenstates opposite to the bulk hopping direction [see Fig. 1(b)], distinct from the NHSE occurring at open boundaries⁵⁵. Such scale-free localization phenomenon is simulated using electrical circuit, as shown in Fig. 2. Here, we set $C_1 = C_2$, $C_v = C_\delta$,

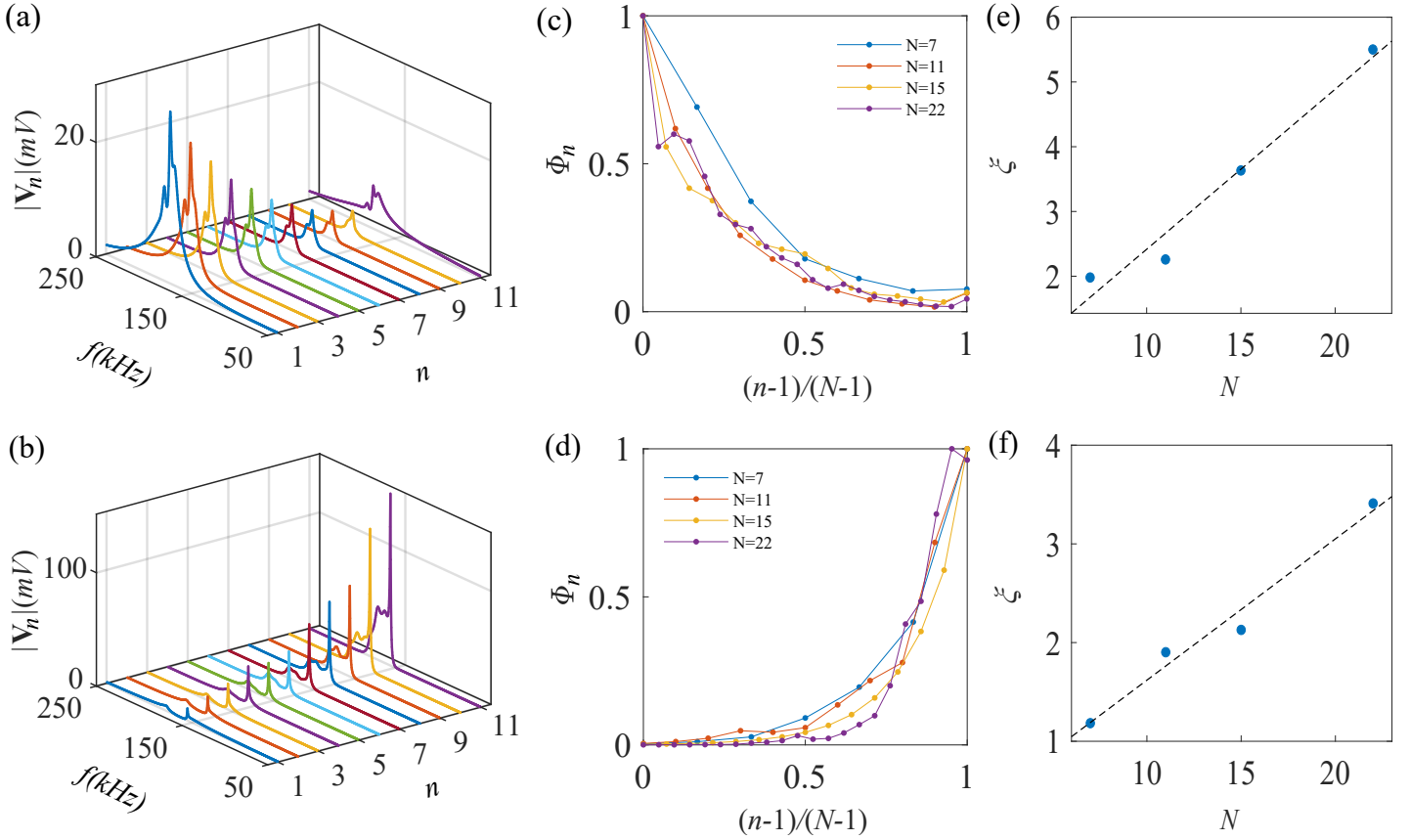


FIG. 2. Simulated results for the scale-free localization in the electrical circuit. Frequency-resolved voltage distribution $|\mathbf{V}_n(\omega)|$ excited by the alternating current (AC) at the different node n (a) for $C_1 = 9.4$ nF and $C_v = 47$ nF, and (b) for $C_1 = 22$ nF and $C_v = 2.2$ nF. (c, d) The corresponding normalized spatial distribution Φ_n of the voltage at different normalized node indices $(n-1)/(N-1)$ for different lattice size N , where the node index is mapped to the range $[0, 1]$. (e, f) Localization length ξ (blue dots) of bulk modes as a function of the lattice size N . The black dashed line denotes a linear fit to ξ .

and introduced onsite disorder through random variations in the fabricated grounded inductors due to imperfect manufacturing processes.

The voltage distribution at resonance frequency can be used to represent the state distribution of the circuit Laplacian. Figure 2(a,b) plots the frequency-resolved voltage distribution $|\mathbf{V}_n(\omega)|$ excited by alternating current (AC) at the different node n for $C_1 = 9.4$ nF and $C_v = 47$ nF, and (b) for $C_1 = 22$ nF and $C_v = 2.2$ nF, corresponding to the skin-mode localized at the left and right sides of the chain, respectively. This indicates that the bulk states localized towards different directions can be controlled by changing the hopping strength within the bulk chain and the the hopping strength at the single-impurity site in spite of the nonreciprocal hopping direction within the bulk.

Figure 1(b) shows the existence of the scale-free localization controlled by the single non-Hermitian impurity in the presence of weak disorder, where the localization length is dependent on the lattice size. In order to demonstrate the scale-free localization, we calculate the normalized spatial distribution Φ_n of the peak voltage at the node n , which is defined as

$$\Phi_n = \frac{\mathbf{V}_n^2|_{\text{peak}}}{\max\{\{\mathbf{V}_1^2|_{\text{peak}}, \mathbf{V}_2^2|_{\text{peak}}, \dots, \mathbf{V}_N^2|_{\text{peak}}\}}}, \quad (6)$$

where $\mathbf{V}_n^2|_{\text{peak}}$ denotes the peak voltage at node n , which is normalized to the maximum value of peak voltages of all the

nodes.

Figure 2(c,d) shows the normalized spatial distribution Φ_n of the peak voltage as a function of the normalized node index $(n-1)/(N-1)$ for the left- and right-localized skin modes at the different lattice size N , where the node index is mapped to the range $[0, 1]$. The state distributions at the different size are collapsed close to each other, indicating the size-dependent localization length. By exponentially fitting the state distribution, we extract the localization length ξ at different lattice size N [see blue dots in Fig. 2(e,f)]. After linearly fitting these dots, the localization length ξ exhibits the linear dependence on the lattice size N . This indicates the existence of the scale-free localization for the skin modes controlled by the single non-Hermitian impurity.

IV. EXPERIMENTAL RESULTS OF ELECTRICAL CIRCUITS

Our main results are the experimental verification of the scale-free localization induced by the single non-Hermitian impurity⁵⁵ using the electrical circuit. The electrical-circuit network and fabricated experimental circuit board are shown in Fig. 1(c,d). As shown in Fig. 1(c), two nodes within the circuit are interconnected via capacitors C_1 and INICs, where the INICs have the equivalent capacitance of $\pm C_2$ in opposite directions. The first and last nodes are connected

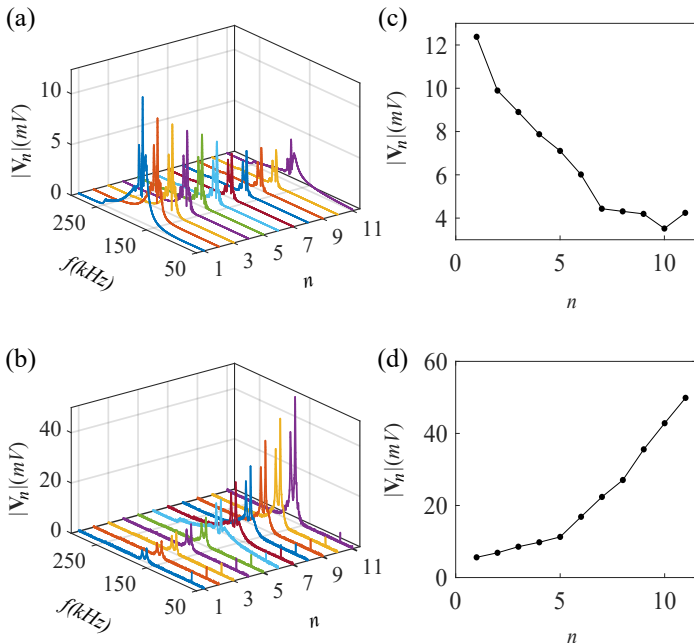


FIG. 3. Experimentally measured voltages of the admittance under chirp signal excitation. Frequency-resolved voltage distribution (a) for $C_1 = 9.4\text{nF}$ and $C_v = 47\text{nF}$, and (b) for $C_1 = 22\text{nF}$ and $C_v = 2.2\text{nF}$, respectively. (c,d) The corresponding spatial distribution of the voltage at the peak frequency, indicating the left-localized and right-localized states.

through distinct capacitors and INICs, denoted as C_v and $\pm C_\delta$, which serve as the single non-Hermitian impurity. The parameters of the experimental electrical circuits are the same as ones used in the simulation. In addition to the random variations suffering from imperfect manufacturing processes, disorder is mainly introduced by the grounded capacitors C_{sn} . The grounded capacitor C_{sn} of each node is randomly chosen from a diverse set of capacitors with capacitance ranging from 0 to $C_S = 10\text{ nF}$. The diagonal element of the circuit Laplacian is given by $1/(i\omega L_0) + i\omega(C_0 + 2C_1 + C_S/2)$, and the circuit's reference frequency reads $f_0 = (2\pi)^{-1}(C_0 + 2C_1 + C_S/2)^{-1/2}L_0^{-1/2}$, where the capacitance C_1 is $C_1 = 9.4\text{ nF}$ for the left-localized states, corresponding to $f_0 = 176\text{ kHz}$, and it is $C_1 = 22\text{ nF}$ for the right-localized states, corresponding to $f_0 = 164.5\text{ kHz}$. A chirp signal spanning the frequency band from 0 kHz to 250 kHz is used as the excitation. Details of the sample fabrication and experimental measurements are provided in the Appendix B.

The experimentally measured voltages of the admittance under the excitation of chirp signals are shown in Fig. 3. We have experimentally designed two electrical circuits with different parameters of boundary capacitors acting as the single impurity, where the bulk parameters are fixed. To be specific, for the $C_1 = 9.4\text{nF}$ and $C_v = 47\text{nF}$, we plot the frequency-resolved voltage distribution [see Fig. 3(a)]. The voltage is peaked around the frequency of 172.5 kHz, which matches well with the simulated result. By extracting the peak voltage at each node, its spatial distribution is shown in Fig. 3(b)], corresponding to the state distribution of non-Hermitian Hamiltonian \mathcal{H} for the specific eigenvalue. This state is localized at the left side, indicating the occurrence of NHSE. While, for $C_1 = 22\text{nF}$ and $C_v = 2.2\text{nF}$, the

voltage is peaked around the frequency of 164 kHz [see Fig. 3(b)], where we observe the right-side localized state [see Fig. 3(d)]. The experimental results indicate the existence of the anomalous skin-mode localization controlled by the single impurity in spite of the bulk hopping direction.

To verify the scale-free localization property, we measured the site-resolved peak voltages for different sizes, as shown in Fig. 4(a,b). For the left-side skin modes, the parameter of the impurity for all the samples is set as $C_1 = 9.4\text{nF}$ and $C_v = 47\text{nF}$, and for the right-side skin modes, it is $C_1 = 22\text{nF}$ and $C_v = 2.2\text{nF}$. Figure 4(a) plots the peak voltages of different samples as a function of normalized node index $(n-1)/(N-1)$, where the node index is normalized to the range $[0, 1]$. These left-side skin modes are not collapsed, indicating the absence of scaled localization for $C_1 = 9.4\text{nF}$ and $C_v = 47\text{nF}$. There is also absence of scaled localization for right-side skin modes with the single-impurity parameters set as $C_1 = 22\text{nF}$ and $C_v = 2.2\text{nF}$. After performing a linear fit of the localization length at different sizes, we observe scale-free localization behavior. This size-dependence of the localization behavior exhibits a significant deviation from the NHSE, where the localization length remains consistent for different system size N , as predicted in Refs.^{31,55}. This unique phenomena of scale-free eigenstates are usually accompanied by the emergence of complex eigenspectrum³¹, which has also been presented in Fig. 4(e,f).

V. CONCLUSION

In summary, we have experimentally observed the anomalous non-Hermitian skin effects with skin-mode localization directions controlled by a single non-Hermitian impurity in non-Hermitian disordered electrical circuits. Furthermore, anomalous skin modes are verified to show the scale-free localization induced by the single non-Hermitian impurity by measuring the size-dependent localization length. Our experimental results have proved the theoretical proposal on the scale-free localization induced by the single non-Hermitian impurity. In the future, it would be interesting to investigate scale-free localization in higher dimensions.

ACKNOWLEDGMENTS

T.L. acknowledges the support from the Fundamental Research Funds for the Central Universities (Grant No. 2023ZYGXZR020), Introduced Innovative Team Project of Guangdong Pearl River Talents Program (Grant No. 2021ZT09Z109), and the Startup Grant of South China University of Technology (Grant No. 20210012). W.B.J is supported by the National Natural Science Foundation of China (NSFC) (Grant No. U21A2093).

Appendix A: Circuit Laplacian

Linear circuit networks, composed of linear components, can be characterized by a series of time-dependent differential equations. After applying the Fourier transformation with respect to the time, these equations can be simplified into a set of algebraic equations in the frequency domain⁶⁴.

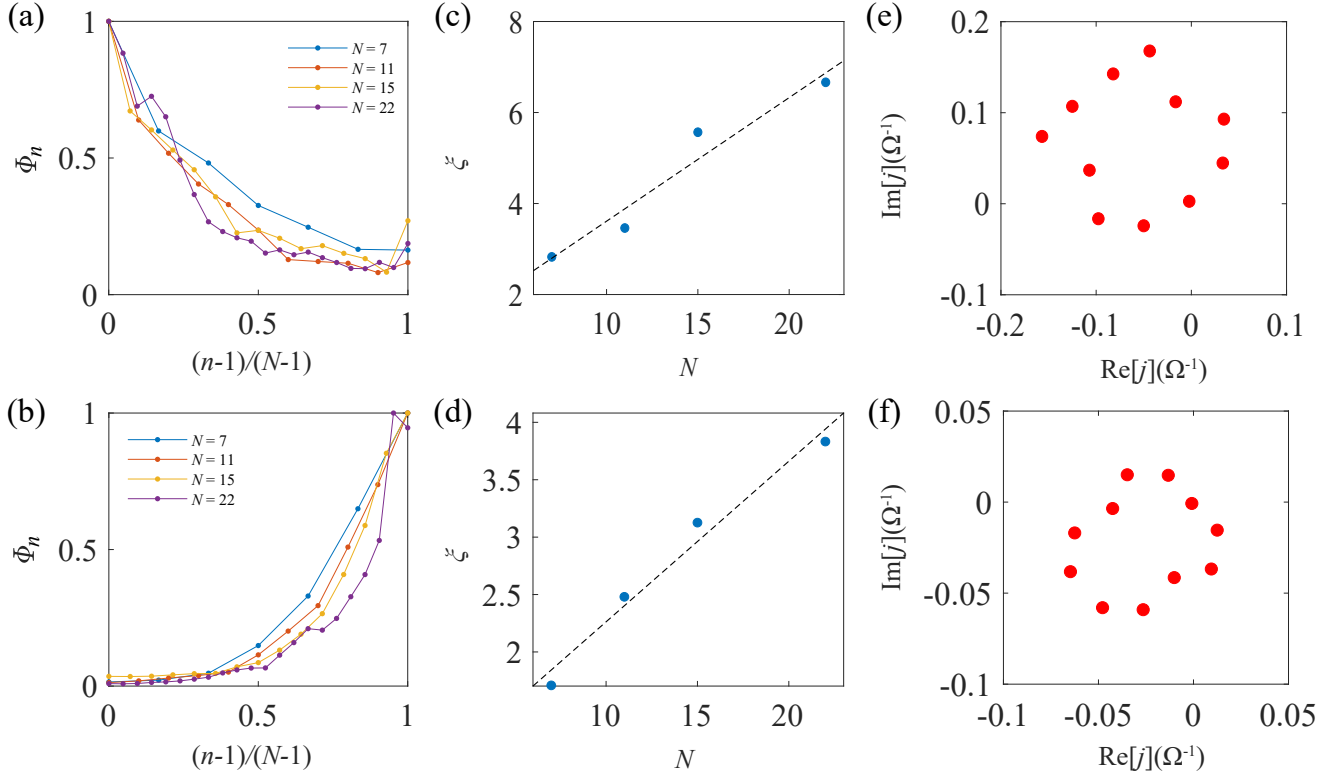


FIG. 4. Experimentally measured scale-free localization in electrical circuit. (a, b) Normalized spatial distribution Φ_n of the voltage at different normalized node index $(n-1)/(N-1)$ for the different lattice size N , where the node index is mapped to the range $[0, 1]$. Here, (a) for $C_1 = 9.4\text{nF}$ and $C_v = 47\text{nF}$, and (b) for $C_1 = 22\text{nF}$ and $C_v = 2.2\text{nF}$. (c, d) Localization length ξ (blue dots) of bulk modes as a function of the lattice size N . The black dashed line denotes a linear fit to ξ . The measured eigenvalues of the admittance (e) for $C_1 = 9.4\text{nF}$ and $C_v = 47\text{nF}$, and (f) for $C_1 = 22\text{nF}$ and $C_v = 2.2\text{nF}$.

In the frequency domain, the relation of current and voltage between two nodes can be written as

$$I_{jk}(\omega) = \frac{V_j(\omega) - V_k(\omega)}{Z_{jk}(\omega)}, \quad (\text{A1})$$

where $Z_{jk}(\omega)$ is the impedance between node j and node k , and the impedances of capacitor, inductor and resistor are $Z_C(\omega) = 1/i\omega C$, $Z_L(\omega) = i\omega L$ and $Z_R(\omega) = R$. According to Kirchhoff's current law, the sum of all currents entering and leaving a node equals zero. This indicates that the input current I_j at the node j equals the sum of the currents leaving node j .

$$I_j = \sum_k I_{jk}. \quad (\text{A2})$$

According to Eq. (A1) and Eq. (A2), we can derive the circuit Laplacian of the electrical circuit in Fig. 1(c,d). Two nearest-neighbor nodes are connected through capacitor with the capacitance $C_1 \pm C_2$, and grounded by a capacitor C_0 , C_{sn} , an inductance L_0 and a resistance R_0 . Two nearest-neighbor nodes are also connected through an INIC in parallel. The INIC acts as a capacitance of $\pm C_2$ in two opposite directions. The circuit equation of the n th

($n \neq 1, N$) node is written as,

$$I_n = \left(i\omega C_0 + i\omega C_{sn} + \frac{1}{i\omega L_0} + R_0 \right) V_n + i\omega(C_1 + C_2)(V_n - V_{n-1}) + i\omega(C_1 - C_2)(V_n - V_{n+1}). \quad (\text{A3})$$

The first and last nodes are connected via the capacitor with the capacitance $C_v \pm C_\delta$, grounded by the capacitor C_L , C_{s1} , an inductance L_0 and a resistance R_0 . The circuit equations for the first and last nodes can be written as

$$I_1 = \left(i\omega C_L + i\omega C_{s1} + \frac{1}{i\omega L_0} + R_0 \right) V_1 + i\omega(C_v + C_\delta)(V_1 - V_N) + i\omega(C_1 - C_2)(V_1 - V_2), \quad (\text{A4})$$

and

$$I_N = \left(i\omega C_R + i\omega C_{sN} + \frac{1}{i\omega L_0} + R_0 \right) V_N + i\omega(C_1 + C_2)(V_N - V_{N-1}) + i\omega(C_v - C_\delta)(V_N - V_1). \quad (\text{A5})$$

In order to have the same on-site potential for all the nodes, we set $C_L = C_1 + C_2 - C_v - C_\delta + C_0$ and $C_R = C_1 - C_2 - C_v + C_\delta + C_0$. Then, we achieve the circuit Laplacian as

$$J = i\omega \begin{pmatrix} C_{s1} - \frac{C_S}{2} - \varepsilon(\omega) & -C_1 + C_2 & 0 & \dots & 0 & -C_v - C_\delta \\ -C_1 - C_2 & C_{s2} - \frac{C_S}{2} - \varepsilon(\omega) & -C_1 + C_2 & \dots & 0 & 0 \\ 0 & -C_1 - C_2 & C_{s3} - \frac{C_S}{2} - \varepsilon(\omega) & \dots & 0 & 0 \\ \vdots & \vdots & \vdots & \ddots & \vdots & \vdots \\ 0 & 0 & 0 & \dots & C_{sN-1} - \frac{C_S}{2} - \varepsilon(\omega) & -C_1 + C_2 \\ -C_v + C_\delta & 0 & 0 & \dots & -C_1 - C_2 & C_{sN} - \frac{C_S}{2} - \varepsilon(\omega) \end{pmatrix}, \quad (\text{A6})$$

where $\varepsilon(\omega) = 1/(\omega^2 L_0) - 2C_1 - C_0 - C_S/2 + i/(\omega R_0)$, and C_{sn} is the grounded capacitance ranging from 0 to C_S , serving as disorder. If we set $\pm C_2 - C_1 = t \pm \gamma$, $\pm C_\delta - C_v = v \pm \delta$, and $C_{sn} - C_S/2 = V_n$, J and \mathcal{H} can be related by $J = i\omega[\mathcal{H} - \varepsilon(\omega)]$.

Appendix B: Details of experimental implementation

1. Experimental setup

The disordered Hatano-Nelson model in the presence of a single non-Hermitian impurity is simulated by the grounded circuit Laplacian J of the electrical circuit in Fig. 1(c). The fabricated circuit board is shown in Fig. 5(a), where the nonreciprocal hopping is realized via utilizing the impedance converters with current inversion (INIC) [see Fig. 5(b)]. The circuit board of each unit cell is shown in Fig. 5(c), where the red dashed curve indicates the INIC.

As shown in Fig. 1(c), two nodes within the circuit are interconnected via capacitors C_1 and INICs, where the INICs exhibit equivalent capacitance of $\pm C_2$ in opposite directions. The first and last nodes are connected through distinct capacitors and INICs, denoted as C_v and $\pm C_\delta$, which serve as the single impurity. Each node is grounded by an inductor $L_0 = 4.7\mu\text{H}$, a resistor R_0 , and capacitors $C_0 = 150\text{ nF}$ and C_{sn} . In addition to the random variations suffering from imperfect manufacturing processes, the random on-site potential is mainly realized by disordered grounded capacitors with the capacitance C_{sn} of each node. The value of C_{sn} is randomly selected within the range from $C_S = 0\text{ nF}$ to $C_S = 10\text{ nF}$.

The diagonal element of the circuit Laplacian is given by $1/(i\omega L_0) + i\omega(C_0 + 2C_1 + C_S/2)$, which vanishes at frequency $f_0 = (2\pi)^{-1}(C_0 + 2C_1 + C_S/2)^{-1/2}L_0^{-1/2}$. In the experimental designs, the capacitance C_1 is chosen as $C_1 = 9.4\text{ nF}$ for the left-localized states, corresponding to $f_0 = 176\text{ kHz}$. It is $C_1 = 22\text{ nF}$ for the right-localized states, corresponding to $f_0 = 164.5\text{ kHz}$. They show good consistency with the experimentally measured frequencies at the maximum voltage response, which were 172.5 kHz and 164 kHz , respectively.

For our specific experimental setup, a circuit board with capacitors, inductors and resistors and operational amplifier was implemented on a Printed Circuit Board (PCB). To ensure proper operation, the operational amplifier (LT1363) was powered by a DC current using the Keysight E3631A power supply. To reduce noise from the DC power supply, capacitors with capacitances of $2.2\mu\text{F}$ and $1\mu\text{F}$ were placed at the DC input of the operational amplifier. A chirp signal, covering a frequency range from 0 kHz to 250 kHz , was generated using a Keysight 33500B waveform generator. The voltage source was interfaced with the Printed Circuit Board

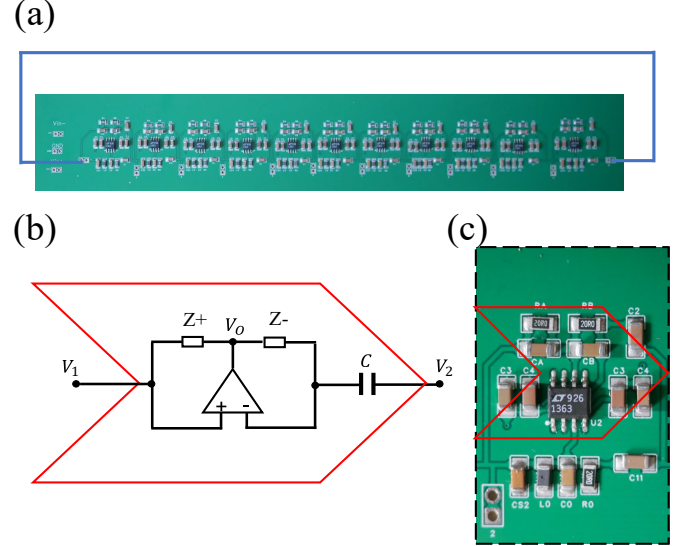


FIG. 5. (a) Experimental circuit board diagram containing eleven unit cells for each board. Multiple boards can be connected to create a longer chain. The first node and the last node are connected by the external wires acting as the single impurity. The nonreciprocal hopping between nodes n and $n+1$ is realized by the negative impedance converters through current inversions (INICs) in (b), where INIC consists of capacitor, resistor and operational amplifier. (c) Circuit board of each unit cell, where the red dashed curve indicates the INIC.

(PCB) through a shunt resistor $R = 51\ \Omega$, functioning as the current input. A current source was input into the PCB to capture the voltage response using a Keysight DSOX4052A oscilloscope. A Fast Fourier Transform (FFT) was then applied to the measured time-domain voltage to obtain the voltage response in the frequency domain.

2. Measurement

In this section, we introduce the measurement of observables in electrical circuits^{65,70}. In our experiment, we measured the circuit's voltage response and complex admittance. In following, we will discuss their correlation with the eigenvectors and eigenvalues of the Laplacian J .

Voltage response—Based on $I = JV$, upon the input of the current, the voltage response at each node can be obtained by the inversion of Laplacian J .

$$V = J^{-1}I = \sum_n \frac{1}{j_n} |\psi_n^R\rangle \langle \psi_n^L|I\rangle, \quad (\text{B1})$$

where j_n is the n th eigenvalue of J , and $|\psi_n^R\rangle$ is the right eigenvector of J with eigenvalue j_n while $\langle \psi_n^L|$ is the left

eigenvector of J . It indicates that all eigenstates contributes to voltage response, where each eigenstate's contribution is weighted by its corresponding admittance j_n and $\langle \psi_n^L | I \rangle$. The eigenvalue $j_n(\omega)$ varies with frequency ω . Assuming that, at the specific frequency, J has the eigenvalue very close to zero, the weight $\langle \psi_n^L | I \rangle / j_n$ of the right eigenvector $|\psi_n^R\rangle$ can be considered significantly larger than contributions from the other right eigenvectors. In this case, the voltage response behaves as

$$V \sim \frac{\langle \psi_n^L | I \rangle}{j_n} |\psi_n^R\rangle. \quad (\text{B2})$$

It indicates that, at this frequency, the voltage response V of the circuit can be considered determined by the eigenvector $|\psi_n^R\rangle$.

Complex admittance— The voltage response depends on

the inverse of the Laplacian $G = J^{-1}$ and input current. Their relationship can be expressed as

$$V = GI, \quad (\text{B3})$$

G is the inverse of the Laplacian J . If we input a current at the single node j , the the voltage response:

$$V_i = G_{ij}I_j. \quad (\text{B4})$$

While we input a current at one node and measure the voltage response of all nodes, one can obtain a column of the matrix G . By repeating this process N times, we obtain G . Consequently, the Laplacian J can be achieved by inverting G . The complex admittance is calculated using the reconstructed Laplacian J .

* These authors contributed equally

† E-mail: liutao0716@scut.edu.cn

‡ E-mail: juwenbo@scut.edu.cn

¹ Y. Ashida, Z. Gong, and M. Ueda, “Non-Hermitian physics,” *Adv. Phys.* **69**, 249 (2020).

² Tony E. Lee, “Anomalous edge state in a non-Hermitian lattice,” *Phys. Rev. Lett.* **116**, 133903 (2016).

³ D. Leykam, K. Y. Bliokh, C. Huang, Y. D. Chong, and F. Nori, “Edge modes, degeneracies, and topological numbers in non-Hermitian systems,” *Phys. Rev. Lett.* **118**, 040401 (2017).

⁴ Y. Xu, S. T. Wang, and L. M. Duan, “Weyl exceptional rings in a three-dimensional dissipative cold atomic gas,” *Phys. Rev. Lett.* **118**, 045701 (2017).

⁵ Z. Gong, Y. Ashida, K. Kawabata, K. Takasan, S. Higashikawa, and M. Ueda, “Topological phases of non-Hermitian systems,” *Phys. Rev. X* **8**, 031079 (2018).

⁶ R. El-Ganainy, K. G. Makris, M. Khajavikhan, Z. H. Musslimani, S. Rotter, and D. N. Christodoulides, “Non-Hermitian physics and PT symmetry,” *Nat. Phys.* **14**, 11 (2018).

⁷ S. Yao and Z. Wang, “Edge states and topological invariants of non-Hermitian systems,” *Phys. Rev. Lett.* **121**, 086803 (2018).

⁸ K. Zhang, Z. Yang, and C. Fang, “Correspondence between winding numbers and skin modes in non-Hermitian systems,” *Phys. Rev. Lett.* **125**, 126402 (2020).

⁹ K. Yokomizo and S. Murakami, “Non-Bloch band theory of non-Hermitian systems,” *Phys. Rev. Lett.* **123**, 066404 (2019).

¹⁰ S. Yao, F. Song, and Z. Wang, “Non-Hermitian Chern bands,” *Phys. Rev. Lett.* **121**, 136802 (2018).

¹¹ F. K. Kunst, E. Edvardsson, J. C. Budich, and E. J. Bergholtz, “Biorthogonal bulk-boundary correspondence in non-Hermitian systems,” *Phys. Rev. Lett.* **121**, 026808 (2018).

¹² T. Liu, Y.-R. Zhang, Q. Ai, Z. Gong, K. Kawabata, M. Ueda, and F. Nori, “Second-order topological phases in non-Hermitian systems,” *Phys. Rev. Lett.* **122**, 076801 (2019).

¹³ F. Song, S. Yao, and Z. Wang, “Non-Hermitian skin effect and chiral damping in open quantum systems,” *Phys. Rev. Lett.* **123**, 170401 (2019).

¹⁴ Y.-T. Zhang, S. Jiang, Q. Li, and Q.-F. Sun, “An analytical solution for quantum scattering through a PT-symmetric delta potential,” *Front. Phys.* **16**, 43503 (2021).

¹⁵ J. Y. Lee, J. Ahn, H. Zhou, and A. Vishwanath, “Topological correspondence between Hermitian and non-Hermitian systems: Anomalous dynamics,” *Phys. Rev. Lett.* **123**, 206404 (2019).

¹⁶ K. Kawabata, T. Bessho, and M. Sato, “Classification of exceptional points and non-Hermitian topological semimetals,” *Phys. Rev. Lett.* **123**, 066405 (2019).

¹⁷ G. Sun, J.-C. Tang, and S.-P. Kou, “Biorthogonal quantum criticality in non-Hermitian many-body systems,” *Front. Phys.* **17**, 33502 (2021).

¹⁸ Z. Y. Ge, Y. R. Zhang, T. Liu, S. W. Li, H. Fan, and F. Nori, “Topological band theory for non-Hermitian systems from the Dirac equation,” *Phys. Rev. B* **100**, 054105 (2019).

¹⁹ H. Zhou and J. Y. Lee, “Periodic table for topological bands with non-Hermitian symmetries,” *Phys. Rev. B* **99**, 235112 (2019).

²⁰ H. Zhao, X. Qiao, T. Wu, B. Midya, S. Longhi, and L. Feng, “Non-Hermitian topological light steering,” *Science* **365**, 1163 (2019).

²¹ K. Kawabata, K. Shiozaki, M. Ueda, and M. Sato, “Symmetry and topology in non-Hermitian physics,” *Phys. Rev. X* **9**, 041015 (2019).

²² D. S. Borgnia, A. J. Kruchkov, and R.-J. Slager, “Non-Hermitian boundary modes and topology,” *Phys. Rev. Lett.* **124**, 056802 (2020).

²³ T. Liu, J. J. He, T. Yoshida, Z.-L. Xiang, and F. Nori, “Non-Hermitian topological Mott insulators in one-dimensional fermionic superlattices,” *Phys. Rev. B* **102**, 235151 (2020).

²⁴ L. Li, C. H. Lee, S. Mu, and J. Gong, “Critical non-Hermitian skin effect,” *Nat. Commun.* **11**, 5491 (2020).

²⁵ K. Yokomizo and S. Murakami, “Scaling rule for the critical non-Hermitian skin effect,” *Phys. Rev. B* **104**, 165117 (2021).

²⁶ N. Okuma, K. Kawabata, K. Shiozaki, and M. Sato, “Topological origin of non-Hermitian skin effects,” *Phys. Rev. Lett.* **124**, 086801 (2020).

²⁷ Y.-Y. Zou, Y. Zhou, L.-M. Chen, and P. Ye, “Detecting bulk and edge exceptional points in non-Hermitian systems through generalized Petermann factors,” *Front. Phys.* **19**, 23201 (2023).

²⁸ A. Fan and S.-D. Liang, “Complex energy plane and topological invariant in non-Hermitian systems,” *Front. Phys.* **17**, 33501 (2021).

²⁹ Y. Yi and Z. Yang, “Non-Hermitian skin modes induced by on-site dissipations and chiral tunneling effect,” *Phys. Rev. Lett.* **125**, 186802 (2020).

³⁰ T. Liu, J. J. He, Z. Yang, and F. Nori, “Higher-order Weyl-exceptional-ring semimetals,” *Phys. Rev. Lett.* **127**, 196801 (2021).

³¹ L. Li, C. H. Lee, and J. Gong, “Impurity induced scale-free localization,” *Commun. Phys.* **4**, 42 (2021).

³² E. J. Bergholtz, J. C. Budich, and F. K. Kunst, “Exceptional

- topology of non-Hermitian systems,” *Rev. Mod. Phys.* **93**, 015005 (2021).
- ³³ Y. Li, C. Liang, C. Wang, C. Lu, and Y.-C. Liu, “Gain-loss-induced hybrid skin-topological effect,” *Phys. Rev. Lett.* **128**, 223903 (2022).
- ³⁴ K. Zhang, Z. Yang, and C. Fang, “Universal non-Hermitian skin effect in two and higher dimensions,” *Nat. Commun.* **13**, 2496 (2022).
- ³⁵ R. Lin, T. Tai, L. Li, and C. H. Lee, “Topological non-Hermitian skin effect,” *Front. Phys.* **18**, 53605 (2023).
- ³⁶ Z. Ren, D. Liu, E. Zhao, C. He, K. K. Pak, J. Li, and G.-B. Jo, “Chiral control of quantum states in non-Hermitian spin-orbit-coupled fermions,” *Nat. Phys.* **18**, 385 (2022).
- ³⁷ K. Kawabata, T. Numasawa, and S. Ryu, “Entanglement phase transition induced by the non-Hermitian skin effect,” *Phys. Rev. X* **13**, 021007 (2023).
- ³⁸ K. Zhang, C. Fang, and Z. Yang, “Dynamical degeneracy splitting and directional invisibility in non-Hermitian systems,” *Phys. Rev. Lett.* **131**, 036402 (2023).
- ³⁹ C.-A. Li, B. Trauzettel, T. Neupert, and S.-B. Zhang, “Enhancement of second-order non-Hermitian skin effect by magnetic fields,” *Phys. Rev. Lett.* **131**, 116601 (2023).
- ⁴⁰ J. Liu, Z.-F. Cai, T. Liu, and Z. Yang, “Reentrant non-Hermitian skin effect in coupled non-Hermitian and Hermitian chains with correlated disorder,” [arXiv:2311.03777](https://arxiv.org/abs/2311.03777) (2023).
- ⁴¹ Z.-F. Cai, T. Liu, and Z. Yang, “Non-Hermitian skin effect in periodically driven dissipative ultracold atoms,” *Phys. Rev. A* **109**, 063329 (2024).
- ⁴² X. Li, J. Liu, and T. Liu, “Localization-delocalization transitions in non-Hermitian Aharonov-Bohm cages,” *Front. Phys.* **19**, 33211 (2024).
- ⁴³ Y.-M. Hu, H.-Y. Wang, Z. Wang, and F. Song, “Geometric origin of non-Bloch \mathcal{PT} symmetry breaking,” *Phys. Rev. Lett.* **132**, 050402 (2024).
- ⁴⁴ H.-Y. Wang, F. Song, and Z. Wang, “Amoeba formulation of non-Bloch band theory in arbitrary dimensions,” *Phys. Rev. X* **14**, 021011 (2024).
- ⁴⁵ X.-D. Xie, Z.-Y. Xue, and D.-B. Zhang, “Variational quantum algorithms for scanning the complex spectrum of non-Hermitian systems,” *Front. Phys.* **19**, 41202 (2024).
- ⁴⁶ H. Zhang, Z. Guo, Y. Li, Y. Yang, Y. Chen, and H. Chen, “A universal non-Hermitian platform for bound state in the continuum enhanced wireless power transfer,” *Front. Phys.* **19**, 43209 (2024).
- ⁴⁷ F. Koch and J. C. Budich, “Quantum non-hermitian topological sensors,” *Phys. Rev. Res.* **4**, 013113 (2022).
- ⁴⁸ J. C. Budich and E. J. Bergholtz, “Non-hermitian topological sensors,” *Phys. Rev. Lett.* **125**, 180403 (2020).
- ⁴⁹ A. McDonald and A. A. Clerk, “Exponentially-enhanced quantum sensing with non-hermitian lattice dynamics,” *Nat. Commun.* **11**, 5382 (2020).
- ⁵⁰ C.-X. Guo, X. Wang, H. Hu, and S. Chen, “Accumulation of scale-free localized states induced by local non-hermiticity,” *Phys. Rev. B* **107**, 134121 (2023).
- ⁵¹ B. Li, H.-R. Wang, F. Song, and Z. Wang, “Scale-free localization and \mathcal{PT} symmetry breaking from local non-hermiticity,” *Phys. Rev. B* **108**, L161409 (2023).
- ⁵² Y. Wang, J. Lin, and P. Xu, “Transmission-reflection decoupling of non-hermitian photonic doping epsilon-near-zero media,” *Front. Phys.* **19**, 33206 (2023).
- ⁵³ Y. Fu and Y. Zhang, “Hybrid scale-free skin effect in non-hermitian systems: A transfer matrix approach,” *Phys. Rev. B* **108**, 205423 (2023).
- ⁵⁴ X. Xie, G. Liang, F. Ma, Y. Du, Y. Peng, E. Li, H. Chen, L. Li, F. Gao, and H. Xue, “Observation of scale-free localized states induced by non-hermitian defects,” *Phys. Rev. B* **109**, L140102 (2024).
- ⁵⁵ P. Mollignini, O. Arandes, and E. J. Bergholtz, “Anomalous skin effects in disordered systems with a single non-Hermitian impurity,” *Phys. Rev. Res.* **5**, 033058 (2023).
- ⁵⁶ W. Zhang, D. Zou, Q. Pei, W. He, J. Bao, H. Sun, and X. Zhang, “Experimental observation of higher-order topological anderson insulators,” *Phys. Rev. Lett.* **126**, 146802 (2021).
- ⁵⁷ W. Zhang, H. Wang, H. Sun, and X. Zhang, “Non-abelian inverse anderson transitions,” *Phys. Rev. Lett.* **130**, 206401 (2023).
- ⁵⁸ S. Imhof, C. Berger, F. Bayer, J. Brehm, L. W. Molenkamp, T. Kiessling, F. Schindler, C. H. Lee, M. Greiter, T. Neupert, and R. Thomale, “Topoelectrical-circuit realization of topological corner modes,” *Nat. Phys.* **14**, 925 (2018).
- ⁵⁹ F. Zangeneh-Nejad and R. Fleury, “Nonlinear second-order topological insulators,” *Phys. Rev. Lett.* **123**, 053902 (2019).
- ⁶⁰ M. Serra-Garcia, R. Süsstrunk, and S. D. Huber, “Observation of quadrupole transitions and edge mode topology in an lc circuit network,” *Phys. Rev. B* **99**, 020304 (2019).
- ⁶¹ W. Zhang, F. Di, X. Zheng, H. Sun, and X. Zhang, “Hyperbolic band topology with non-trivial second chern numbers,” *Nat. Commun.* **14**, 1083 (2023).
- ⁶² W. Zhang, H. Yuan, N. Sun, H. Sun, and X. Zhang, “Observation of novel topological states in hyperbolic lattices,” *Nat. Commun.* **13**, 2937 (2022).
- ⁶³ T. Hofmann, T. Helbig, C. H. Lee, M. Greiter, and R. Thomale, “Chiral voltage propagation and calibration in a topoelectrical Chern circuit,” *Phys. Rev. Lett.* **122**, 247702 (2019).
- ⁶⁴ C. H. Lee, S. Imhof, C. Berger, F. Bayer, J. Brehm, L. W. Molenkamp, T. Kiessling, and R. Thomale, “Topoelectrical circuits,” *Commun. Phys.* **1**, 39 (2018).
- ⁶⁵ T. Helbig, T. Hofmann, C. H. Lee, R. Thomale, S. Imhof, L. W. Molenkamp, and T. Kiessling, “Band structure engineering and reconstruction in electric circuit networks,” *Phys. Rev. B* **99**, 161114 (2019).
- ⁶⁶ Z.-Q. Zhang, B.-L. Wu, J. Song, and H. Jiang, “Topological anderson insulator in electric circuits,” *Phys. Rev. B* **100**, 184202 (2019).
- ⁶⁷ Y. Wang, H. M. Price, B. Zhang, and Y. D. Chong, “Circuit implementation of a four-dimensional topological insulator,” *Nat. Commun.* **11**, 2356 (2020).
- ⁶⁸ J. Bao, D. Zou, W. Zhang, W. He, H. Sun, and X. Zhang, “Topoelectrical circuit octupole insulator with topologically protected corner states,” *Phys. Rev. B* **100**, 201406 (2019).
- ⁶⁹ Y. Lu, N. Jia, L. Su, C. Owens, G. Juzeliūnas, D. I. Schuster, and J. Simon, “Probing the berry curvature and fermi arcs of a weyl circuit,” *Phys. Rev. B* **99**, 020302 (2019).
- ⁷⁰ T. Helbig, T. Hofmann, S. Imhof, M. Abdelghany, T. Kiessling, L. W. Molenkamp, C. H. Lee, A. Szameit, M. Greiter, and R. Thomale, “Generalized bulk-boundary correspondence in non-Hermitian topoelectrical circuits,” *Nat. Phys.* **16**, 747 (2020).